INTERNATIONAL JOURNAL FOR NUMERICAL METHODS IN FLUIDS
Int. J. Numer. Meth. Fluids 2010; **63**:600–621
Published online 9 June 2009 in Wiley InterScience (www.interscience.wiley.com). DOI: 10.1002/fld.2092

Turbulent flow simulation using LES with dynamical mixed one-equation subgrid models in complex geometries

Wenquan Wang[1,*,†], Lixiang Zhang[1], Yan Yan[1] and Yakun Guo[2]

[1]*Department of Engineering Mechanics, Kunming University of Science and Technology, Kunming, Yunnan 650051, China*
[2]*School of Engineering, University of Aberdeen, Aberdeen AB24 3UE, U.K.*

SUMMARY

An innovative computational model is presented for the large eddy simulation of multi-dimensional unsteady turbulent flow problems in complex geometries. The main objectives of this research are (i) to better understand the structure of turbulent flows in complex geometry and (ii) to investigate the 3D characteristics of such complex fluid flow. The filtered Navier–Stokes equations are used to simulate large scales of the turbulence, while the energy transfer from large scales to subgrid-scales (SGS) is simulated using dynamical mixed one-equation subgrid models. In the proposed SGS model, the SGS kinetic energy, k_{sgs}, is used for scaling the velocity for the eddy-viscosity part of the model. The proposed SGS model contains not only some information on the small scales as described in traditional Smagorinsky model or Germano dynamical model but also includes additional scale-similarity as that in the models of Ghosal *et al.* (*J. Comput. Phys.* 1995; **118**:24–37) or Davidson (*11th International Symposium on Turbulent Shear Flow*, Grenoble, vol. 3, 1997; 26.1–26.6). The Navier–Stokes equations and the derived k_{sgs} equation are solved using implicit finite-volume method. The models have been applied to simulate the 3D flows over a backward-facing step and in a strong 3D skew runner blade passage of a Francis hydro turbine, respectively. Good agreement between simulated results and experimental results as well as other numerical results was obtained. Copyright © 2009 John Wiley & Sons, Ltd.

Received 11 November 2008; Revised 15 April 2009; Accepted 18 April 2009

KEY WORDS: turbulent flows; large eddy simulation; dynamical one-equation subgrid models; subgrid-scale kinetic energy; finite-volume method; complex geometries

*Correspondence to: Wenquan Wang, Department of Engineering Mechanics, Kunming University of Science and Technology, Kunming, Yunnan 650051, China.
†E-mail: wwqquan@yahoo.com.cn

Contract/grant sponsor: National Natural Science Foundation of China (NSFC); contract/grant numbers: 50839003, 50579025

1. INTRODUCTION

Turbulent flows are of great practical interest in many environmental and engineering fields and may be defined as a 3D flow with highly disordered, intermittent and rotational fluid motion and with diffusive and dissipative characteristics. Owing to its practical importance, extensive studies have been carried out and some reliable results have been obtained [1–4].

Many numerical techniques, such as Direct Numerical Simulation (DNS), Large Eddy Simulation (LES) and Reynolds Averaged Navier–Stokes (RANS), have been applied for the simulation of turbulence flows. DNS can give the most accurate simulation results. However, for flows with high Reynolds numbers, where the influence of the different turbulence scales must be taken into account, it is difficult to apply DNS due to the enormous requirement for computational resources and unknowns involved in the computational solution. So far, DNS is only suitable to be used for simulating the low Reynolds number flow with relative simple flow passage. RANS models are often used to simulate the turbulent flows in many industrial fields. This approach is based on the separation of the instantaneous value of a specific flow variable in its mean value and fluctuations with respect to this mean value. The well-known Reynolds stress components are originated substituting mean values and fluctuations of the variables in the conservation equations. However, RANS model induces more unknowns than equations, thus, various turbulence models are developed to describe the Reynolds stress components and to close the equations. These closure models contain many empirical parameters that are determined from specific examples, thus the application of RANS is limited.

LES is currently a popular tool for the simulation of turbulence flows. This methodology was initially proposed by Smagorinsky [5], and it consists of the separation of the large eddies and subgrid-scales (SGS) using a grid filter. Large eddies are associated with the low flow frequencies and are originated by the domain geometry and the boundaries. SGS are associated with the high frequencies and have an isotropic and homogeneous behavior, and can maintain their independence with respect to the main stream. In LES the large eddies are simulated directly, whereas SGS are simulated using closure models. This approach shows that it can significantly improve the computational accuracy compared with RANS while keeping the computational cost relatively lower compared with DNS.

The energy transfer between large and small scales is mainly between the scales closest to the cut-off. The scale-similarity models [6] are established based on this argument. These models use the correlation between the smallest resolved scales and the largest unresolved scales in LES to model the main part of the SGS energy. They are always used together with some dissipative model such as the Smagorinsky model, e.g. the mixed models. In early simulations using mixed models [6, 7], the constant in the Smagorinsky model was prescribed *a priori*. The dynamical SGS model was developed by Germano *et al.* [8] and Lilly [9]. However, the velocity scales in their model only contain the information for the large scales. Zang *et al.* [10] used this model in the dynamic mode to simulate recirculation flows. The SGS model is capable of covering a large part of the turbulent kinetic energy to make LES a practical tool for complex flows at high Reynolds numbers. Though a large part of the SGS energy is modeled with the scale-similarity approach, a significant amount of the SGS energy in a coarse LES is still simulated using the Smagorinsky model [11]. The Smagorinsky model assumes the isotropy of the small scales. Obviously this model is not suitable for modeling a significant part of the SGS energy resulting from the scales with obvious anisotropic characteristics. It does not contain any information on the SGS energy. The SGS velocity scale of the Smagorinsky model, $|\bar{S}| = (2\bar{S}_{ij}\bar{S}_{ij})^{1/2}$, is strongly

DOI: 10.1002/fld

affected by the mean flow. On the other hand, the smallest unresolved scales are assumed not to be correlated with the large scales. It is apparent that a more suitable model containing some information about the SGS energy is needed for modeling the smallest SGS scales in turbulence flows.

This paper presents a mixed dynamic model in which the SGS kinetic energy model is used as a dissipative part in the model. The dynamic models based on the k_{sgs} proved to give an accurate representation of the unresolved scales in a coarse LES [12–17]. They are more robust than the Germano's model and allow transfer of turbulent energy from small to large scales. Furthermore, the velocity scale, $k_{sgs}^{1/2}$, in the mixed models contains some information on the small scales, and the solution of the transport equations for k_{sgs} contributes to a history effect in the model. It has been shown that the model is Galilean invariant and realizable. Moreover, the approximately correct near-wall behavior of the model has been proven [18]. The model was tested for both channel flow and for the case of a surface-mounted cube, it was found that the model gave accurate results for both cases [19].

Though LES has been successfully applied to simulate the turbulence flows with complex geometry [20–22], relatively few studies have been reported using LES for simulating the flow in a strong three-dimensional (3D) skew Francis hydro-turbine passage. A few studies of DNS and LES of fully turbulent flow in a low pressure turbine passage have been done, only for two-dimensional (2D) blade cascade simplifications [23–25]. As an important turbo-machinery for electricity generation by water power, the coming flow at a high velocity, with strongly distorted wakes due to stay and guide vanes, passes through the blade passage at the entrance with an angle of attack. The high curvature walls enforce the flow to change direction, inducing a quite complicated non-uniform and unsteady turbulent flow. So far, numerical simulations of the turbulent flows in the strong 3D skew blade passage for a Francis turbine have mostly been done based on the $k-\varepsilon$ models of RANS for engineering purpose, the mechanisms and the spatial and temporal distributions of turbulence flow in the passage are hardly known. In this paper, we use LES with the dynamical mixed one-equation subgrid models to simulate the complex 3D turbulent flow in a highly curved turbine passage.

2. GOVERNING EQUATIONS

2.1. Description of dynamical mixed one-equation subgrid model

The system of equations to simulate turbulent flows of Newtonian incompressible fluids are given by

$$\frac{\partial u_j}{\partial x_j}=0 \tag{1}$$

$$\frac{\partial u_i}{\partial t}+\frac{\partial}{\partial x_j}(u_i u_j)+\frac{1}{\rho}\frac{\partial p}{\partial x_i}-\frac{\partial}{\partial x_j}\left[\upsilon\left(\frac{\partial u_i}{\partial x_j}+\frac{\partial u_j}{\partial x_i}\right)\right]=0 \tag{2}$$

where u_i and p are the velocity components and pressure, respectively. υ is the molecular kinetic viscosity.

DOI: 10.1002/fld

Applying a grid filter to the continuity and momentum equations, respectively, the following filtered expressions for a Newtonian incompressible fluid are obtained:

$$\frac{\partial \bar{u}_j}{\partial x_j} = 0 \tag{3}$$

$$\frac{\partial \bar{u}_i}{\partial t} + \frac{\partial}{\partial x_j}(\bar{u}_i \bar{u}_j) + \frac{1}{\rho}\frac{\partial \bar{p}}{\partial x_i} - \frac{\partial}{\partial x_j}\left[\upsilon\left(\frac{\partial \bar{u}_i}{\partial x_j} + \frac{\partial \bar{u}_j}{\partial x_i}\right) - \tau_{ij}\right] = 0 \tag{4}$$

where $\bar{u}_i$ and $\bar{p}$ are the filtered velocity components and pressure, respectively. The SGS stress tensor,

$$\tau_{ij} = \overline{u_i u_j} - \bar{u}_i \bar{u}_j \tag{5}$$

is modeled as

$$\tau_{ij}^{\mathrm{M}} = \tau_{ij}^{\mathrm{SS}} + \tau_{ij}^{\mathrm{EV}} \tag{6}$$

Here, the scale-similarity part of the SGS stress tensor is modeled as

$$\tau_{ij}^{\mathrm{SS}} = \overline{\bar{u}_i \bar{u}_j} - \bar{\bar{u}}_i \bar{\bar{u}}_j \tag{7}$$

and the eddy-viscosity part is modeled as

$$\tau_{ij}^{\mathrm{EV}} = -2C(x, y, z, t)\Delta k_{\mathrm{sgs}}^{1/2} \bar{S}_{ij} + \tfrac{2}{3}\delta_{ij} k_{\mathrm{sgs}} \tag{8}$$

where $C(x, y, z, t)$ is a space and time-dependent coefficient, δ_{ij} is Kronecker's delta, $\bar{S}_{ij}$ is the strain-rate tensor on the grid level. Instead of using the velocity scale $|\bar{S}|$, which is common practice in the dynamic models, we use $k_{\mathrm{sgs}}^{1/2}$ as the velocity scale. The advantage for using $k_{\mathrm{sgs}}^{1/2}$ as velocity scale is that the information from the small scales is included in the SGS model through k_{sgs}.

Subtracting the product of $\bar{u}_i$ and Equation (4) from the filtered product of u_i and Equation (2) yields:

$$\overline{u_i \frac{\partial u_i}{\partial t}} - \bar{u}_i \frac{\partial \bar{u}_i}{\partial t} + \overline{u_i \frac{\partial}{\partial x_j}(u_i u_j)} - \bar{u}_i \frac{\partial}{\partial x_j}(\bar{u}_i \bar{u}_j) = -\frac{1}{\rho}\left(\overline{u_i \frac{\partial p}{\partial x_i}} - \bar{u}_i \frac{\partial \bar{p}}{\partial x_i}\right) + \overline{\upsilon u_i \frac{\partial^2 u_i}{\partial x_j \partial x_j}} - \upsilon \bar{u}_i \frac{\partial^2 \bar{u}_i}{\partial x_j \partial x_j} + \bar{u}_i \frac{\partial \tau_{ij}^{M}}{\partial x_j} \tag{9}$$

Assuming that the resolved and the SGS kinetic energy are

$$\bar{k} = \frac{1}{2}\bar{u}_i \bar{u}_i, \quad k_{\mathrm{sgs}} = \frac{1}{2}\tau_{ii}^{\mathrm{EV}} \tag{10}$$

The total kinetic energy can then be modeled as

$$k = \bar{k} + k_{\mathrm{sgs}} + \tfrac{1}{2}\tau_{ii}^{\mathrm{SS}} \tag{11}$$

DOI: 10.1002/fld

Substituting Equations (10) and (11) into Equation (9) and rearranging the equation gives

$$\frac{\partial k_{\mathrm{sgs}}}{\partial t}+\frac{\partial}{\partial x_j}(\bar{u}_j k_{\mathrm{sgs}})=-\tau_{ij}^M\frac{\partial \bar{u}_i}{\partial x_j}-\frac{\partial}{\partial x_j}\left(\frac{1}{2}\overline{u_i u_i u_j}-k\bar{u}_j+\frac{1}{\rho}\overline{u_j p}-\frac{1}{\rho}\bar{u}_j\bar{p}-\bar{u}_i\tau_{ij}^M\right)$$
$$+\upsilon\frac{\partial k_{\mathrm{sgs}}^2}{\partial x_j\partial x_j}-\upsilon\left(\overline{\frac{\partial u_i}{\partial x_j}\frac{\partial u_i}{\partial x_j}}-\frac{\partial \bar{u}_i}{\partial x_j}\frac{\partial \bar{u}_i}{\partial x_j}\right)$$
$$+\left(\upsilon\frac{\partial^2}{\partial x_j\partial x_j}\left(\frac{1}{2}\tau_{ii}^{\mathrm{SS}}\right)-\frac{\partial}{\partial t}\left(\frac{1}{2}\tau_{ii}^{\mathrm{SS}}\right)\right)-\frac{\partial}{\partial x_j}\left(\frac{1}{2}\tau_{ii}^{\mathrm{SS}}\bar{u}_j\right) \tag{12}$$

The SGS diffusion terms in Equation (12) are modeled as

$$D=-\frac{\partial}{\partial x_j}\left(\frac{1}{2}\overline{u_i u_i u_j}-k\bar{u}_j+\frac{1}{\rho}\overline{u_j p}-\frac{1}{\rho}\bar{u}_j\bar{p}-\bar{u}_i\tau_{ij}^M\right)=\frac{\partial}{\partial x_j}\left(\upsilon_{sgs}\frac{\partial k_{\mathrm{sgs}}}{\partial x_j}\right) \tag{13}$$

The dissipation in Equation (12) can be modeled as

$$\varepsilon_{k\mathrm{sgs}}=\upsilon\left(\overline{\frac{\partial u_i}{\partial x_j}\frac{\partial u_i}{\partial x_j}}-\frac{\partial \bar{u}_i}{\partial x_j}\frac{\partial \bar{u}_i}{\partial x_j}\right)=C_\varepsilon\frac{k_{\mathrm{sgs}}^{3/2}}{\Delta} \tag{14}$$

The production term in Equation (12), i.e. the SGS dissipation of the resolved kinetic energy, can be modeled as

$$\Pi=-\tau_{ij}^M\frac{\partial \bar{u}_i}{\partial x_j}=\Pi^{\mathrm{SS}}+\Pi_{k\mathrm{sgs}}=-\tau_{ij}^{\mathrm{SS}}\frac{\partial \bar{u}_i}{\partial x_j}-\tau_{ij}^{\mathrm{EV}}\frac{\partial \bar{u}_i}{\partial x_j} \tag{15}$$

Substitution of Equations (13)–(15) into Equation (12) gives the control equation of the SGS kinetic energy

$$\frac{\partial k_{\mathrm{sgs}}}{\partial t}+\frac{\partial}{\partial x_j}(\bar{u}_j k_{\mathrm{sgs}})=\Pi_{k\mathrm{sgs}}+\frac{\partial}{\partial x_j}\left((\upsilon_{sgs}+\upsilon)\frac{\partial k_{\mathrm{sgs}}}{\partial x_j}\right)-C_\varepsilon\frac{k_{\mathrm{sgs}}^{3/2}}{\Delta}$$
$$+\Pi^{\mathrm{SS}}+\upsilon\frac{\partial^2}{\partial x_j\partial x_j}\left(\frac{1}{2}\tau_{ii}^{\mathrm{SS}}\right)-\frac{\partial}{\partial t}\left(\frac{1}{2}\tau_{ii}^{\mathrm{SS}}\right)-\frac{\partial}{\partial x_j}\left(\frac{1}{2}\tau_{ii}^{\mathrm{SS}}\bar{u}_j\right) \tag{16}$$

Before we can use Equation (16) to simulate the SGS kinetic energy, two important coefficients in Equation (16), i.e. the SGS turbulent viscosity υ_{sgs} and the SGS dissipation coefficient C_ε need to be defined and solved.

The coefficient, $C(x,y,z,t)$, is computed using a dynamic procedure. To this end, we need to define some quantities on the trail test level. Introducing $\hat{\cdot}$ as a test-filter with a filter with of $\hat{\Delta}=2\Delta$, the SGS stress on the test level can be written as $T_{ij}=\widehat{\overline{u_i u_j}}-\hat{\bar{u}}_i\hat{\bar{u}}_j$. Similar to τ_{ij}^{SS} and τ_{ij}^{EV}, T_{ij}^{SS} and T_{ij}^{EV} are introduced, respectively, as the scale-similarity and the eddy-viscosity parts of the modeled SGS stress on the test level, T_{ij}^M, i.e.

$$T_{ij}^M=T_{ij}^{\mathrm{SS}}+T_{ij}^{\mathrm{EV}}=\widehat{\overline{u_i u_j}}-\hat{\bar{u}}_i\hat{\bar{u}}_j \tag{17}$$

DOI: 10.1002/fld

T_{ij}^{SS} and T_{ij}^{EV} are modeled as

$$T_{ij}^{\mathrm{SS}} = \widehat{\bar{u}_i \bar{u}_j} - \hat{\bar{u}}_i \hat{\bar{u}}_j \tag{18}$$

$$T_{ij}^{\mathrm{EV}} = -2C(x, y, z, t)\hat{\Delta} K^{1/2} \hat{\bar{S}}_{ij} + \tfrac{2}{3}\delta_{ij} K \tag{19}$$

where the strain-rate tensor on the test level, $\hat{\bar{S}}_{ij}$, is defined as

$$\hat{\bar{S}}_{ij} = \frac{1}{2}\left(\frac{\partial \hat{\bar{u}}_i}{\partial x_j} + \frac{\partial \hat{\bar{u}}_j}{\partial x_i}\right) \tag{20}$$

The SGS kinetic energy on test level, K, is defined as $K = \frac{1}{2} T_{ii}^{\mathrm{EV}}$.

Applying the Germano identity, i.e.

$$L_{ij} = \widehat{\bar{u}_i \bar{u}_j} - \hat{\bar{u}}_i \hat{\bar{u}}_j = T_{ij} - \hat{\tau}_{ij} \tag{21}$$

substitution of the modeled SGS stress on the test level, T_{ij}^{M}, and the modeled SGS stress on the grid level, τ_{ij}^{M}, into Equation (21), gives

$$L_{ij} - H_{ij} = 2C(x, y, z, t) M_{ij} \tag{22}$$

where

$$H_{ij} = (\widehat{\bar{\bar{u}}_i \bar{\bar{u}}_j} - \hat{\bar{\bar{u}}}_i \hat{\bar{\bar{u}}}_j) \tag{23}$$

$$M_{ij} = \widehat{\Delta k_{\mathrm{sgs}}^{1/2} \bar{S}_{ij}} - \hat{\Delta} K^{1/2} \hat{\bar{S}}_{ij} \tag{24}$$

The square error, $E_{ij} E_{ij} = (L_{ij} - H_{ij} - 2C(x, y, z, t) M_{ij})^2$, is minimized to obtain [9]

$$C(x, y, z, t) = -\frac{1}{2} \frac{(L_{ij} - H_{ij}) M_{ij}}{M_{ij} M_{ij}} \tag{25}$$

The computation reveals that the local coefficient $C(x, y, z, t)$ often yields a highly oscillating eddy-viscosity field including a significant partition with negative values, which destabilizes the numerical calculation. To this end, a homogeneous coefficient $C_{\mathrm{hom}}(t)$ is often used in the practical simulations. $C_{\mathrm{hom}}(t)$ is computed with the requirement that the SGS dissipation of the resolved kinetic energy in the whole computational domain remains the same as with the local coefficient $C(x, y, z, t)$, i.e.

$$\langle 2C(x, y, z, t) \Delta k_{\mathrm{sgs}}^{1/2} \bar{S}_{ij} \bar{S}_{ij} \rangle_{xyz} = 2C_{\mathrm{hom}}(t) \langle \Delta k_{\mathrm{sgs}}^{1/2} \bar{S}_{ij} \bar{S}_{ij} \rangle_{xyz} \tag{26}$$

where $\langle \cdot \rangle_{xyz}$ denotes space averaging over the entire domain.

$C_{\mathrm{hom}}(t)$ is used to define the SGS turbulent viscosity, υ_{sgs}

$$\upsilon_{sgs} = C_{\mathrm{hom}}(t) \Delta k_{\mathrm{sgs}}^{1/2} \tag{27}$$

in Equation (16) and in the momentum equations.

In RANS, Rodi [26] proposed that the convective and diffusive transport of $\overline{u_i u_j}$ is proportional to that of k with the proportionality coefficient being $\overline{u_i u_j}/k$. Following this approach, we use

DOI: 10.1002/fld

a similar assumption to calculate the dissipation coefficient, C_ε, in Equation (16). Assuming that the convective and diffusive transport of the SGS kinetic energy on the grid filter level, k_{sgs}, is proportional to that of the SGS kinetic energy on the test-filter level, K with the proportionality coefficient k_{sgs}/K. Since

$$C_K + D_K = \Pi_K - \Pi_K^{\text{SS}} - \varepsilon_K \tag{28}$$

$$\hat{C}_{k_{\text{sgs}}} + \hat{D}_{k_{\text{sgs}}} = \hat{\Pi}_{k_{\text{sgs}}} - \hat{\Pi}^{\text{SS}} - \hat{\varepsilon}_{k_{\text{sgs}}} \tag{29}$$

with the convection terms C_K and $C_{k_{\text{sgs}}}$ and the diffusion terms D_K and $D_{k_{\text{sgs}}}$, we obtain (note that the scale-similarity terms have been absorbed in the convection and diffusion terms)

$$\frac{k_{\text{sgs}}}{K}(\Pi_K + \Pi_K^{\text{SS}} - \varepsilon_K) = \hat{\Pi}_{k_{\text{sgs}}} + \hat{\Pi}^{\text{SS}} - \hat{\varepsilon}_{k_{\text{sgs}}} \tag{30}$$

where,

$$\Pi_K = -T_{ij}^{\text{EV}} \hat{\bar{S}}_{ij}, \quad \Pi_K^{\text{SS}} = -T_{ij}^{\text{SS}} \hat{\bar{S}}_{ij}, \quad \varepsilon_K = C_\varepsilon \frac{K^{3/2}}{\hat{\Delta}} \tag{31}$$

Thus, we have

$$C_\varepsilon^{n+1} = \left[\Pi_K + \Pi_K^{\text{SS}} - \frac{k_{\text{sgs}}}{K} \left(\hat{\Pi}_{k_{\text{sgs}}} + \hat{\Pi}^{\text{SS}} - C_\varepsilon^n \widehat{\frac{k_{\text{sgs}}^{3/2}}{\Delta}} \right) \right] \frac{\hat{\Delta}}{K^{3/2}} \tag{32}$$

where C_ε^{n+1} denotes the dissipation coefficient for time step $n+1$. The requirement of non-negative viscous dissipation by definition yields $C_\varepsilon \geqslant 0$.

2.2. Numerical method

An implicit finite-volume method is used for solving the incompressible Navier–Stokes equations and modeled k_{sgs} equation. The viscous plus subgrid fluxes are approximated by central differences of second-order accuracy and the convective term is discretized using the scheme of second order upwind. To compare the dissipative effect of the numerical method, the scheme of central differences is also applied to discretize the convective term. The pressure–velocity coupling is realized with the SIMPLEC algorithm. The details on the numerical method can be found in Reference [27].

The top-hat filter is applied in this study. The grid filtering is applied implicitly through the discretization. The explicit filtering at the test level is numerically carried out by assuming linear variation of the variables and integrating over the test cell [10].

The source terms in the numerical solution of Equation (16) are discretized as $S = S_p k_{\text{sgs}} + S_u$ with $S_p = \min(b)/k_{\text{sgs}}$ and $S_u = \max(b)$. Here, b is the scale-similarity terms and the eddy-viscosity production and dissipation terms in Equation (16).

DOI: 10.1002/fld

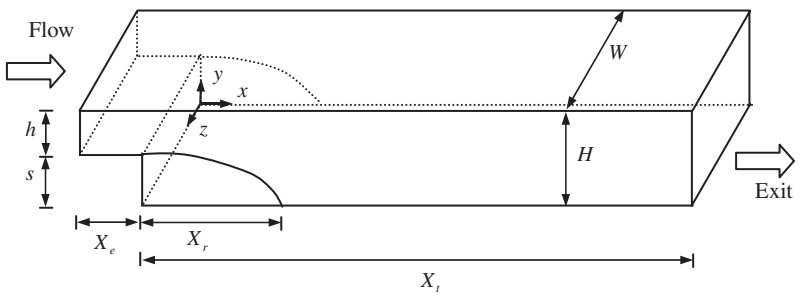

Figure 1. The computational domain.

3. NUMERICAL APPLICATIONS

3.1. 3D flow over a backward-facing step

This numerical example is used to verify the accuracy of our model and to examine the sensitivity of the size of meshes on the simulation results. 3D flows in a backward-facing step are simulated and analyzed. Such a flow is complex and has characteristics of layers separation, reattachment and recirculation. One of the important characteristics is the relation between Reynolds number and the reattachment length. This allows comparison of the results obtained in this work with previous numerical and experimental results obtained by other researchers [28–31].

The computational domain is depicted in Figure 1, where $W=8.0\,\text{cm}$, $h=0.98\,\text{cm}$, $s=1.0\,\text{cm}$, $X_e=20\,\text{cm}$ and $X_t=100\,\text{cm}$. Figure 1 also defines the coordinate system, where the x-, y-, and z-coordinate denote the streamwise, the transverse and the spanwise directions, respectively. There are solid walls at the top, the bottom and the two sides of the channel. Non-slip boundary conditions were applied at the solid walls. At the channel exit only pressure was prescribed ($P=0$). At the channel entrance the velocity profile corresponds to a fully developed flow, perpendicular to the entrance plane. The inflow velocity profile is given by

$$U(y)=\frac{2}{3}U_{\max}\left[1-\left(\frac{y-s-h/2}{s+h/2}\right)^2\right] \tag{33}$$

where $U_{\max}$ is the maximum velocity.

The Reynolds number for this problem is defined as [29]

$$Re=\frac{4U_{\max}Wh}{3\upsilon(W+h)} \tag{34}$$

For the 3D flow, a mesh with six-faced hexahedron elements was constructed. To investigate the effect of the size of mesh on the simulation, two calculations are carried out for the resolution of $420\times42\times80$ (Case 1) and $300\times28\times40$ (Case 2) in the x, y and z directions, respectively. Uniform meshes are used on the upstream section from the step in the streamwise direction, while non-uniform meshes with a first/last spacing ratio $\lambda=1:2.5$ are used on the downstream section from the step in the streamwise direction. Non-uniform meshes with a Bi-exponent distribution are used in transverse and the spanwise directions to take into account the effects of the near wall.

DOI: 10.1002/fld

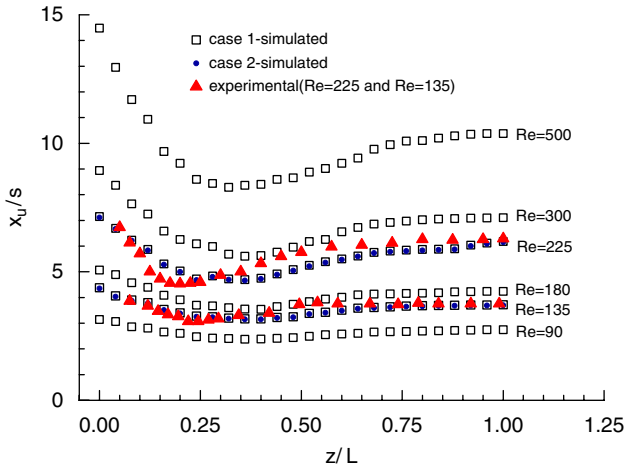

Figure 2. Comparison between measured and simulated x_u-lines at $y/s = 0.05$ (low Reynolds number flow).

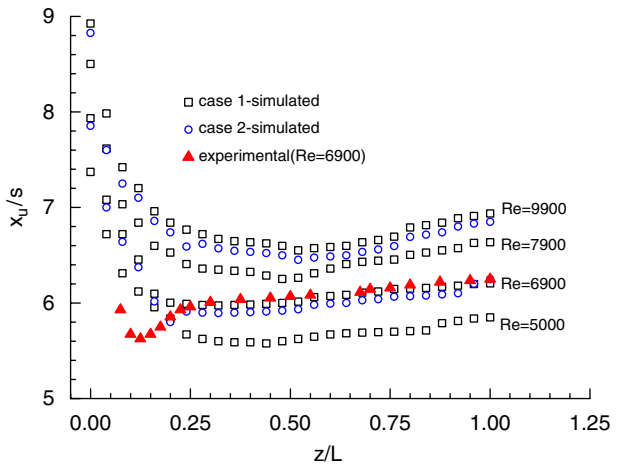

Figure 3. Comparison between measured and simulated x_u-lines at $y/s = 0.05$ (turbulent flow).

Numerical simulation of the mean streamwise velocity component (u) is carried out on planes adjacent to the bounding walls downstream from the step (i.e. the stepped wall, the sidewall and the flat wall). The mean streamwise locations where the velocity component is equal to zero are determined. These locations are used to identify the x_u-line distribution, defined in the same way as in Reference [31]. Comparisons between the numerical simulation and the measured x_u-lines on a plane adjacent to the stepped wall ($y/s = 0.05$) by Nie and Armaly [31] are presented for both low and high Reynolds number flows in Figures 2 and 3, respectively. It can be seen that the size of the reverse flow regions increases and moves further downstream in the low Reynolds number flow regime, decreases and moves upstream in the transitional flow regime, and rises up again in the turbulent flow regime as the Reynolds number increases.

DOI: 10.1002/fld

The spanwise distribution of the boundary line for the reverse flow region adjacent to the stepped wall becomes a minimum near the sidewall in the low Reynolds number flow regime, but that minimum in the distribution disappears in the turbulent flow regime. These figures clearly demonstrate the behavior of these boundary lines as a function of the Reynolds numbers. Good agreement between the numerical simulation and measurements was obtained for low Reynolds number flow, while simulated flow field reasonably agreed with the measurements for high Reynolds number flow, indicating that the numerical method presented here can accurately simulate the turbulent flows with a range of Reynolds numbers. It is also seen that the size of grids has little effect on the numerical simulation for low Reynolds number flow and has a slight influence on simulation for flows with high Reynolds number.

3.2. The turbulent flow in a Francis hydro-turbine passage

3.2.1. Computational setup. The second numerical example is a runner blade of a test Type-A55x Francis hydro-turbine model. The computational domain, including the distributor (a stay vane and a guide vane) and the runner, is shown in Figure 4. The distributor domain corresponds to an inter-blade channel that is bounded upstream by a cylindrical patch A–A and downstream by a conical patch B–B. The distributor inlet section corresponds to the spiral casing outlet section, while the distributor outlet section is conventionally considered to be the distributor–runner interface. The runner corresponds to an inter-blade channel that is bounded upstream by a conical patch (wrapped on the same conical surface as the distributor outlet), then across the runner middle axis C–C, and extends downstream up to the draft tube inlet of radius D–D. The separation of the made-up turbulence is caused by the strong 3D skewing passage. The geometry is normalized by the half external diameter of the runner blade, $R_{\text{ref}} = 0.225\,\text{m}$. The mean chord dimension L of the runner blade passage (streamwise dimension) is $L/R_{\text{ref}} = 0.724$, the mean blade-pitch dimension is $y/R_{\text{ref}} = 0.46$ and the mean spanwise dimension of the blade passage is $z/R_{\text{ref}} = 2.06$ The mean coming flow velocity at the inlet of the runner domain (B–B) passage is defined as reference velocity $U_{\text{ref}} = 0.68\,\text{m/s}$. The flow Reynolds number is defined as $Re = U_{\text{ref}} L/v^f = 1.1 \times 10^5$.

The meshes around the runner blade surfaces are first generated and then the other domains are generated in turn. The tetrahedral fluid element number of the whole model is 1 957 828 and 11 160 nodes are distributed over one side of the blade surfaces (averaging 90 points in the streamwise direction and 124 points in the spanwise direction). The nearest wall grid cell is 12 wall units in the blade-pitch direction and 80 wall units in the other two directions.

The computational boundary conditions are shown in Figure 4 and are presented as following. A uniform velocity field that is normal at the inflow section is imposed on the distributor inlet section. The turbulence quantities are prescribed on the inflow section of the distributor by vortex method [32]. The free outflow condition is specified on the runner outlet (draft tube inlet). The periodic conditions are imposed on the pitchwise periodic boundary, and noslip wall conditions are imposed on all solid boundaries, namely the stay vane, guide vane, runner blade and distributor upper and lower rings as well as on the crown and band surfaces of the runner blade.

A strategy of varying time interval is adopted during the numerical calculation to speed up the convergence and ensure computational accuracy. The maximum time step is controlled to be less than $2.0 \times 10^{-3} T$ ($T = L/U_{\text{ref}}$ as the passing period of the blade passage). The grid turbulence simulation has progressed to $20T$ and collection of the sampling data for time statistics starts from $4T$.

DOI: 10.1002/fld

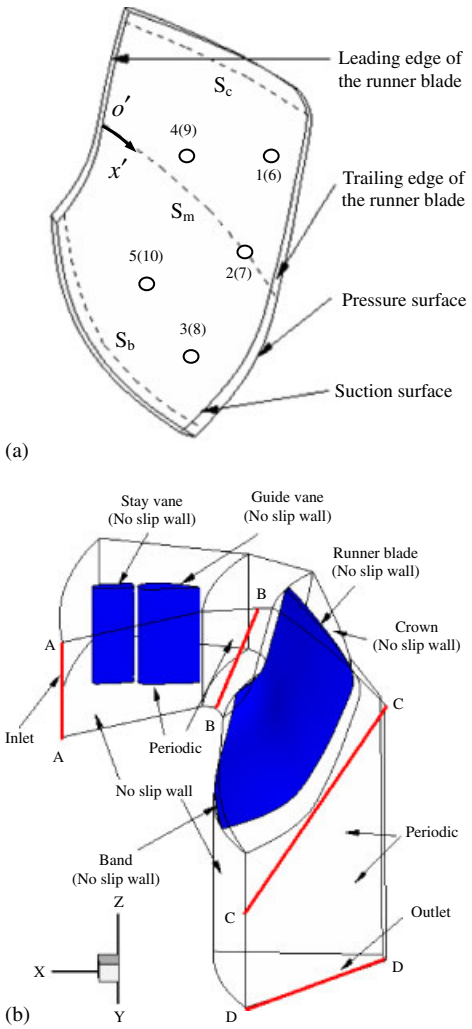

Figure 4. The geometric configuration, computational domain, and boundary conditions. (a) The configuration of a blade and (b) the whole configuration of the flow passage.

3.2.2. Numerical results.

3.2.2.1. Statistic characteristics. The time-averaged static pressure coefficients, $C_p = 2(\bar{p} - \bar{p}_{\text{out}})/\rho U_{\text{ref}}^2$, along the suction and pressure sides of the blade are shown in Figure 5(a), where $\bar{p}_{\text{out}}$ is the mean static pressure in the draft tube inlet section of radius D–D The time-averaged skin friction coefficients, $C_{\text{f}} = 2\tau_{\text{w}}/\rho U_{\text{ref}}^2$, along the suction and pressure sides of the blade are shown in Figure 5(b), where τ_w is the wall shear stress. It is seen that the pressure distribution along the S_c, S_m and S_b lines on the pressure surface shows similar characters. The figure shows that a short region of reverse pressure gradient occurs from the leading edge to $x'/L = 0.18$ or so.

DOI: 10.1002/fld

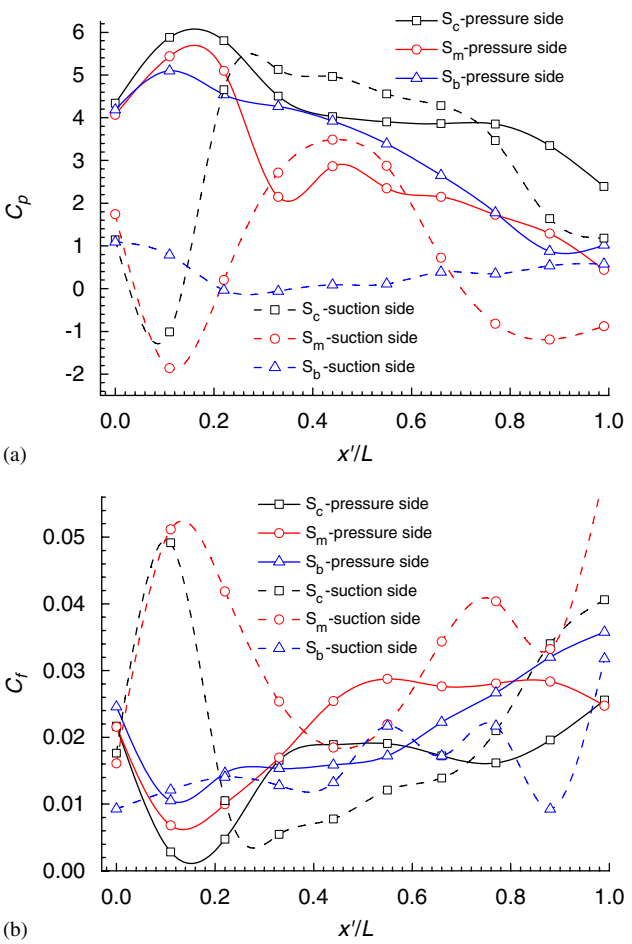

Figure 5. Averaged pressure (a) and skin friction coefficient distribution (b) on blade surface.

The pressure then gradually decreases towards the trailing edge. However, the pressure distribution along the S_c, S_m and S_b lines on the suction side greatly differs from each other. Along the S_c, S_m lines, a short region of acceleration is seen at the leading zone of the passage. After a short decelerated from $x'/L=0.1$ to $x'/L=0.25$, a high-pressure gradient occurs until the trailing edge of the blade. The pressure gradient along the S_b is quite different. It is seen that a reverse pressure gradient occurs from $x'/L=0.2$ toward the trailing edge of the blade. The flow direction may be changed due to reverse pressure gradient, which leads to a low skin friction coefficient, flow separation and instability. These features are demonstrated and verified furthermore in Figure 5(b).

Figure 6(a), (b) shows the contours of pressure and velocity distributions in the 3D skew blade passage, respectively. It clearly shows the space distribution of pressure and velocity which is useful to help understand the process of flow evolvement. Figure 6(a), (b) shows that there is a

DOI: 10.1002/fld

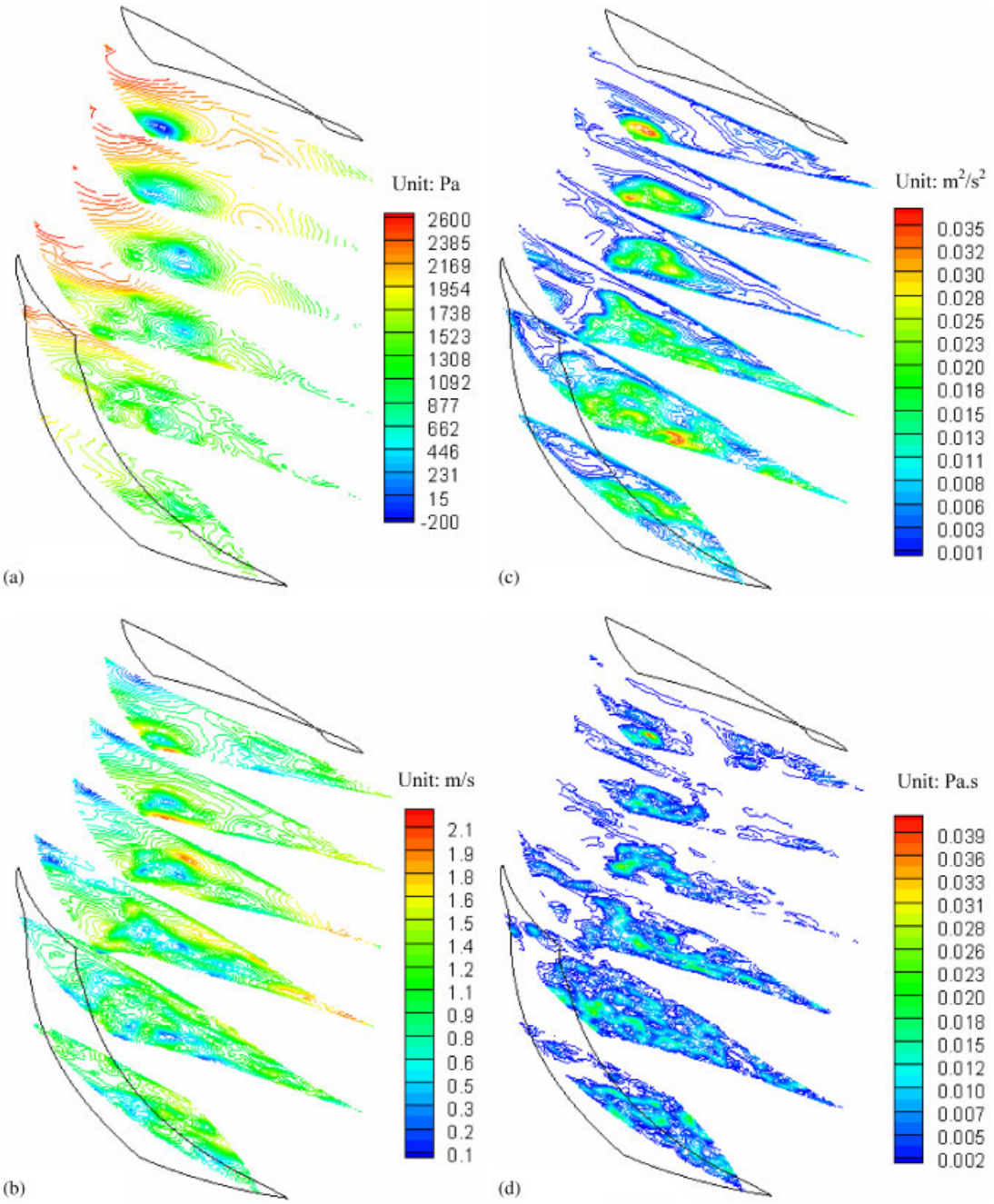

Figure 6. Time-averaged pressure, velocity, SGS kinetic energy and SGS turbulent viscosity distribution in blade passage. (a) Pressure; (b) Velocity; (c) SGS kinetic energy; and (d) SGS turbulent viscosity.

DOI: 10.1002/fld

high-pressure zone near the leading edge of the blade in the pressure side and the pressure gradient is nearly the same along the stream lines in the crown zones. Near the suction surface, a negative pressure center occurs near the crown, which suggests that there is a strong collective swirling vortex. It is also seen that the contours of the pressure are relatively mess if near the band zone, indicating that the strong collective vortex in crown zone is continuous to split into some small vortex pairs entered into the band zone and the vortex intensity starts to decrease from the leading edge toward the trailing edge of the blade.

Figure 6(c),(d) shows the contours of time-averaged SGS kinetic energy and SGS turbulent viscosity distribution in blade passage, respectively. The space distribution of SGS kinetic energy and dissipation of turbulent kinetic energy demonstrates the mechanics of products and dissipation of turbulent energy.

3.2.2.2. Temporal evolution. Figure 7 shows the instantaneous iso-surface of spanwise vorticity in the blade passage at different times. These figures clearly show the unsteady evolvement of swirling vortex structures. A strong clockwise spanwise vortex is seen in the leading zone. The vortex is then gradually elongated with time and eventually is broken. As a result, many small vortex pairs are generated and move into the band zone. The distances between vortex pairs increase with time and its intensity gradually decreases. Finally, the flow becomes unstable. This is consistent with the pressure patterns shown in Figure 5(a).

Figure 8 shows the evolution of computational SGS kinetic energy at some points on two sides of blade (numbered 1–10 in Figure 4(a)). It is seen that the subgrid kinetic energy and its fluctuation are slightly higher than the subtest kinetic energy and its fluctuation. This demonstrates the difference of energy transport due to the different eddy scales. Figure 8 also shows that the SGS kinetic energy varies with spacious locations, indicating that the eddy scales induced by skew blade are different.

The time variation of homogeneous coefficient $C_{\mathrm{hom}}(t)$ is plotted in Figure 9(a). It is seen that the time-averaged $C_{\mathrm{hom}}(t)$ is close to 0.022, which corresponds to a value of the Smagorinsky constant $Cs = 0.2$. There is no negative value of $C_{\mathrm{hom}}(t)$. The local coefficient $C(x, y, z, t)$ at points 1, 4, 6, 9 is plotted in Figure 9(b), which shows larger fluctuation and more stochastic compared with the homogeneous coefficient $C_{\mathrm{hom}}(t)$, because it is local.

3.2.2.3. Experiments and comparisons. Details of the experimental arrangement and the test model can be found in Reference [1]. For completeness and convenience, we give a brief description of the test model. The turbine used for the experiments is a model of a Francis turbine, A55x. The model runner diameter is 450 mm, with 10 blades, 23 guide vanes and 23 stay vanes. The test model is made of hard polyglass with Young's modulus of 2500 MPa, Poisson ratio of 0.384 and a mass density of $1280\,\mathrm{kg/m^3}$. The net working water head and the rotation velocity can be adjusted according to the requirements of experiments. Pressure sensors, LL-072-25A, were mounted on both the pressure side (numbered 15) and the suction side (numbered 610) of a blade to record the turbulent pressure signal. The locations of the sensors are shown in Figure 4(a) in which the pressure sensors were arranged in a way that they were roughly placed along the streamwise direction. The sampling resolution is 2.5 kHz for flow.

Figure 10 is the comparison of computed and measured time-averaged pressures. Two simulations were carried out using the second-order upwind and central difference schemes to discretize the convective term in the governing equations, respectively. Though the numerical results show

DOI: 10.1002/fld

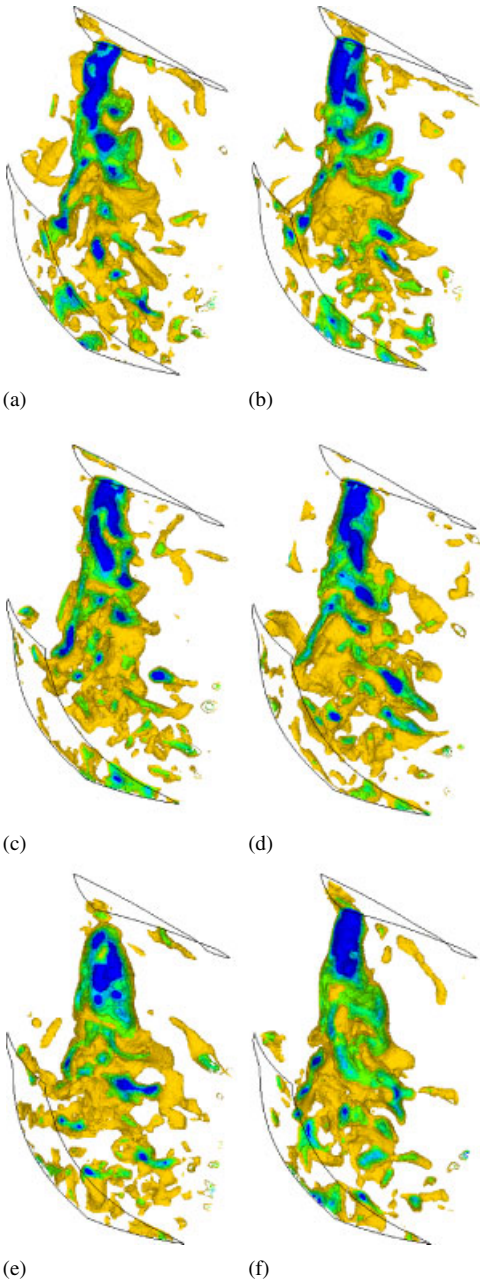

Figure 7. Contours of iso-surface of spanwise vorticity in blade passage. From black to French grey: $-110\ 1/s \leqslant \omega_z \leqslant -30\ 1/s$. (a) $\frac{t}{T} = 17.66$; (b) $\frac{t}{T} = (18.07)$; (c) $\frac{t}{T} = 18.48$; (d) $\frac{t}{T} = 18.89$; (e) $\frac{t}{T} = 19.3$; and (f) $\frac{t}{T} = 19.71$.

DOI: 10.1002/fld

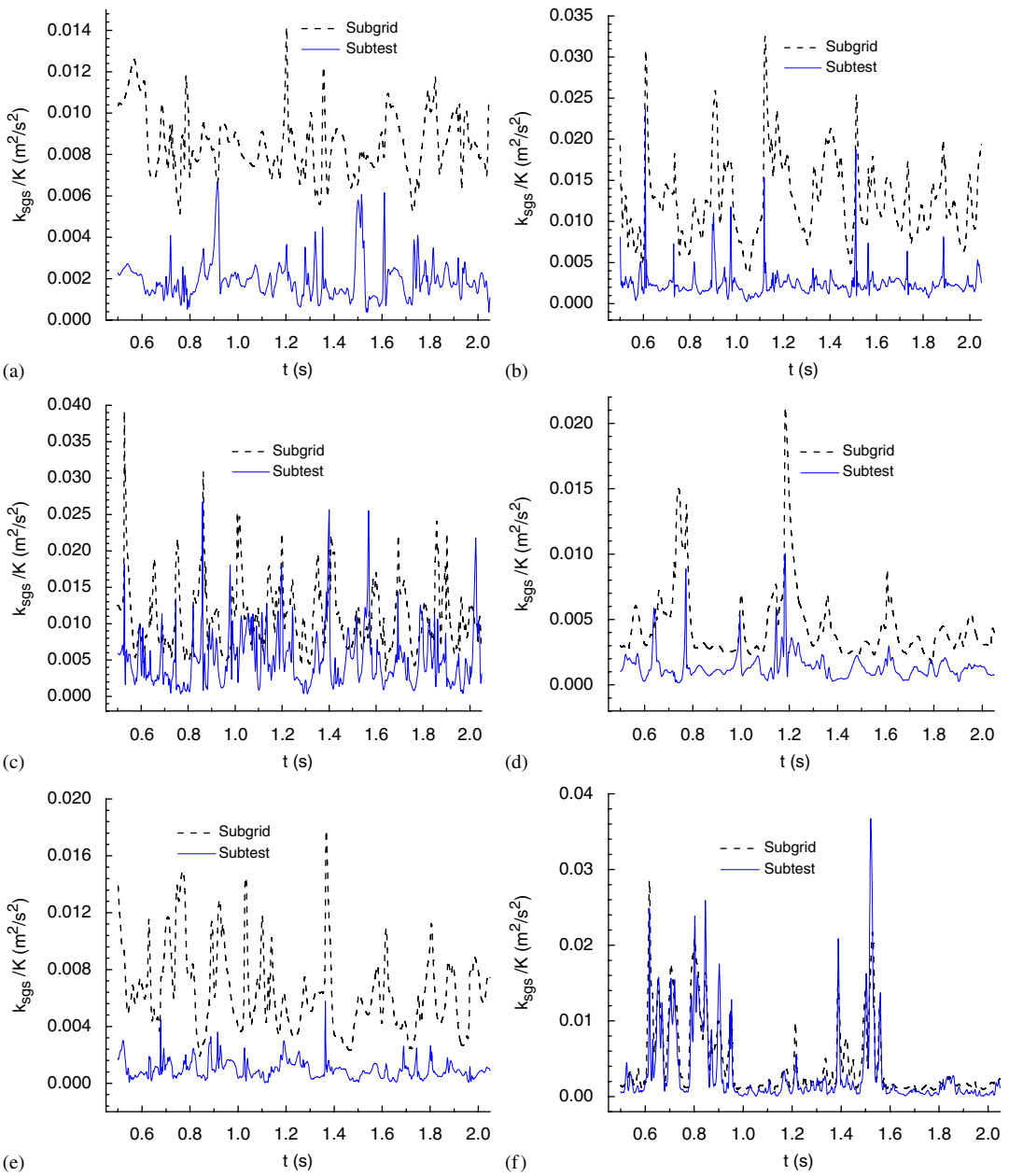

Figure 8. The evolution of the computational SGS kinetic energy on grid and test level on two sides of the blade, respectively. (a) Point 1; (b) Point 2; (c) Point 3; (d) Point 4; (e) Point 5; (f) Point 6; (g) Point 7; (h) Point 8; (i) Point 9; and (j) Point 10.

DOI: 10.1002/fld

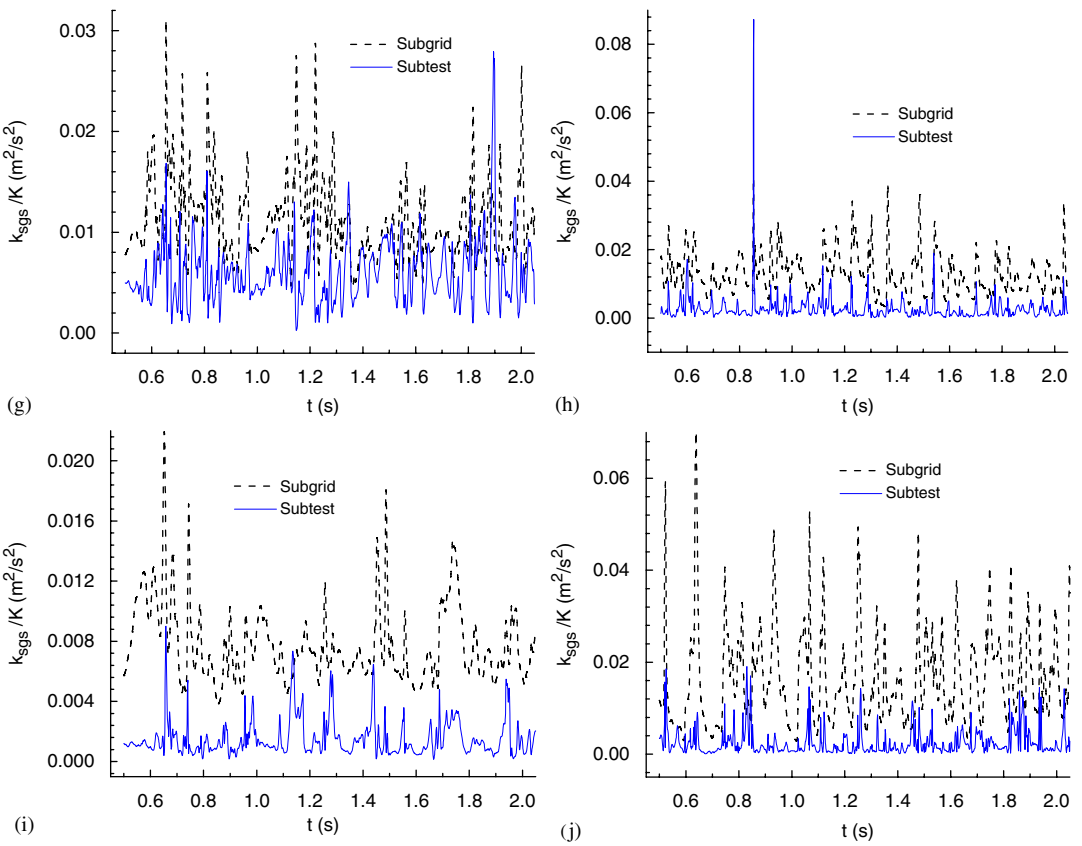

Figure 8. *Continued*.

slight difference using different schemes of discretization for convective term, the numerical (non-physical) dissipation of two schemes is of the same order of magnitude. In general, the simulated time-averaged pressures agree well with the measurements with the maximum relative error being about 8% (point 8 at suction side) indicating that the LES with the dynamical mixed one-equation subgrid models is reliable in complex turbulence computation.

Figure 11 is the computed and measured time-dependent pressures at the measured points. The recorded signals were treated with five wavelet decompositions of the DB4 wavelet function in order to obtain smooth curves for the purpose of comparison. Both the computed and measured results show that the pressure fluctuation frequency is relatively higher near the band regions than that near the crown regions, and that of the upstream zones are slightly higher than that in the downstream zones. This may be ascribed mainly to the difference of the eddy scales. Large-scale eddies are main collection in the upstream zones of the runner passage affected by the big attack angle of guide vane, while the small scale eddies are filled in the downstream flow passage with the collective large vortex structure broken, which agree well with the vortex structure shown in Figure 7. It is also seen that the amplitude of pressure

DOI: 10.1002/fld

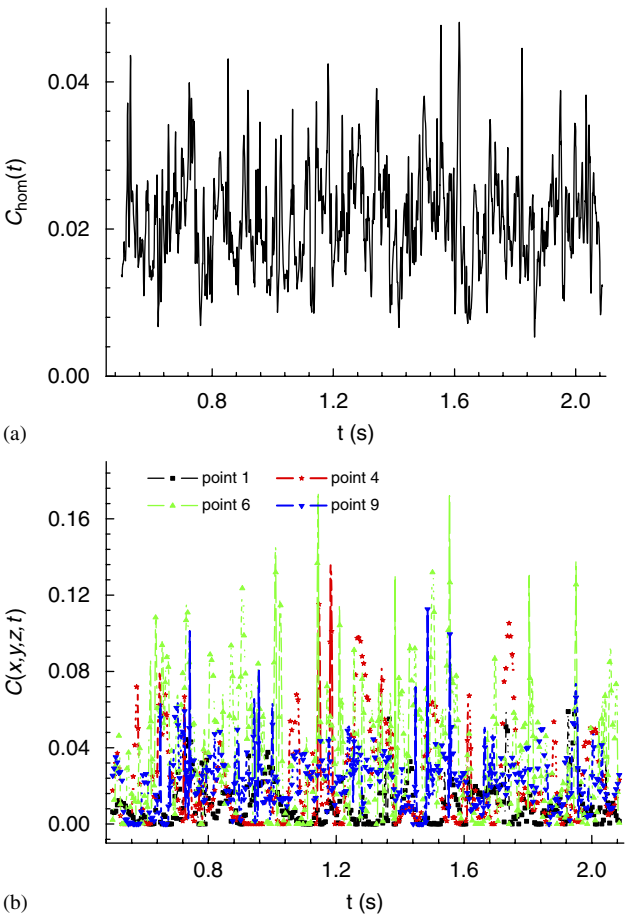

Figure 9. The evolution of the dynamical coefficients: (a) the homogeneous coefficient C_{hom}(t); (b) the local coefficient C(x, y, z, t).

fluctuation is different between the computation and the measurement, which may be caused by the difference of boundary condition between the numerical computation and the physical experiments.

4. CONCLUSION

A computational model is developed for the LES modeling with dynamical mixed one-equation subgrid model. This model is more robust than the Germano model and is capable of simulating the transfer of turbulent energy from small to large scales. Furthermore, the velocity scale, $k_{sgs}^{1/2}$, in the mixed models contains some information on the small scales, and the solution of the

DOI: 10.1002/fld

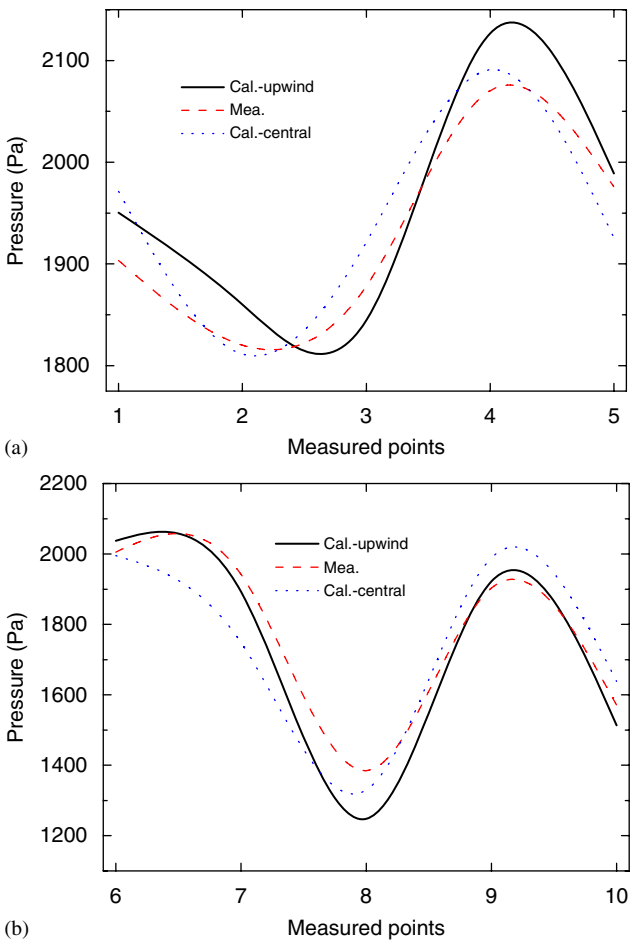

Figure 10. Comparisons of time-averaged computed and measured pressures. (a) Pressure side; (b) Suction side.

transport equations for k_{sgs} contributes a history effect. Based on the SIMPLEC schemes for the coupled terms of velocity and pressure, this model is implemented in a 3D finite volume code. Two numerical examples are simulated. The first one is to simulate the 3D flows over a backward-facing step. Simulated results were compared with the experimental results [31]. Good agreement between the simulation and the measurements was obtained for relatively low Reynolds number flows while a reasonable agreement was achieved for turbulent flow, indicating that the numerical model presented here can be used to simulate a wide range flow regimes. The second numerical example is to simulate the complex turbulent flow in a strong 3D skew Francis hydro-turbine passage. The statistic characteristics of pressure, velocity, SGS kinetic energy and SGS turbulent viscosity are numerically simulated. The evolvements of spatial–temporal vortex structures, the temporal subgrid kinetic energy and the subtest kinetic energy are calculated and analyzed. The simulated pressures on the pressure and suction sides of the blade agree well with the measurements, indicating the

DOI: 10.1002/fld

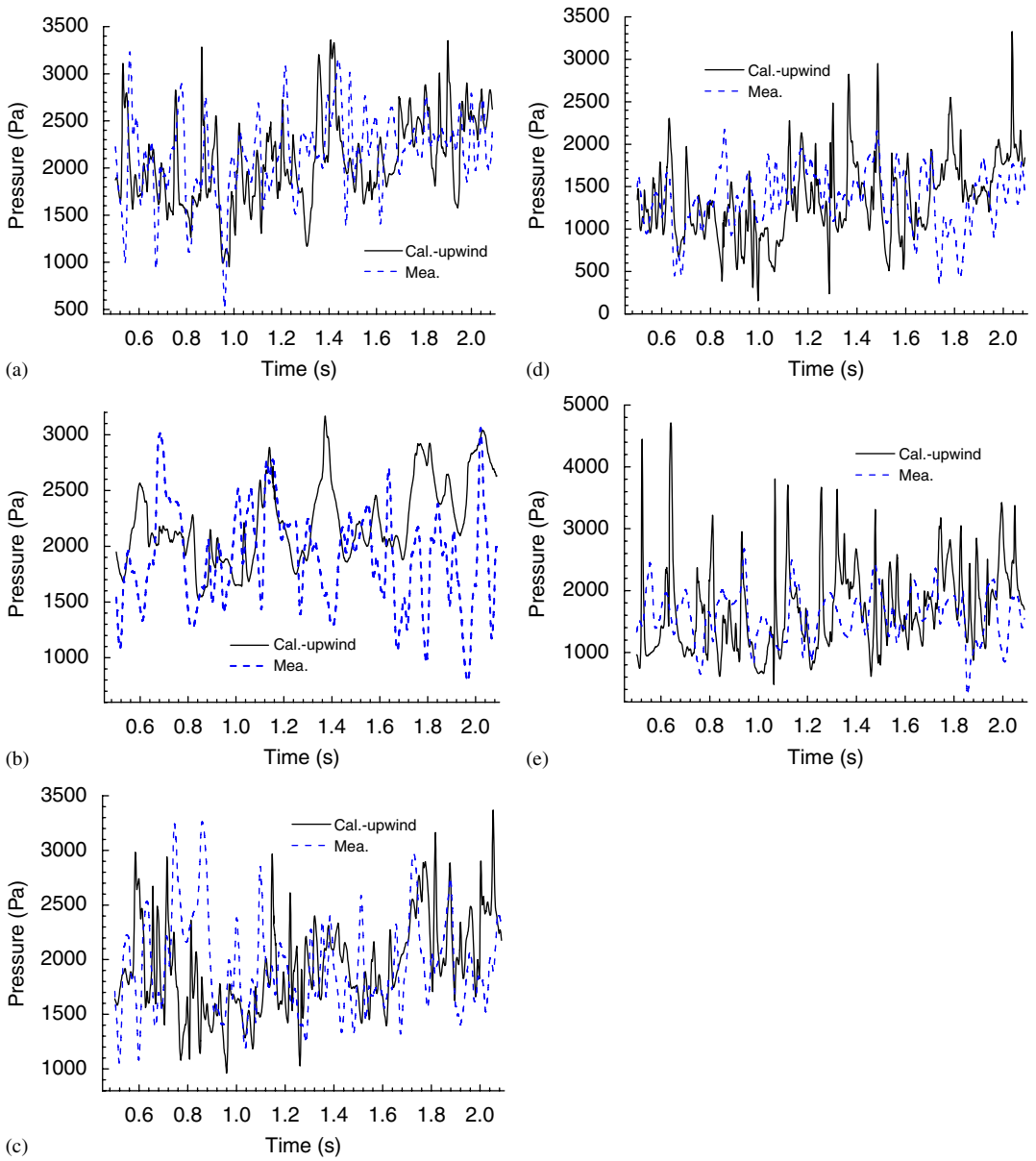

Figure 11. History comparisons of total pressure at measured points on two sides of blade.

accuracy of the numerical model. The findings from this research improve our understanding of the mechanism of turbulent flow, energy production and dissipation as well as the turbulent coherent structure in turbine machines.

DOI: 10.1002/fld

ACKNOWLEDGEMENTS

The authors thank the National Natural Science Foundation of China (NSFC) [Key Program: 50839003 and General Program: 50579025] for financial support of this research. Comments of reviewers' greatly improve the quality of the paper.

REFERENCES

1. Zhang LX, Guo Y, Wang WQ. Large eddy simulation of turbulent flow in a true 3D Francis hydro turbine passage with dynamical fluid–structure interaction. *International Journal for Numerical Methods in Fluids* 2007; **54**:517–541.
2. Liew KM, Wang WQ, Zhang LX, He XQ. A computational approach for predicting hydroelasticity of flexible structures based on the pressure Poisson equation. *International Journal for Numerical Methods in Engineering* 2007; **72**(13):1560–1583.
3. Wang WQ, Zhang LX, Yan Y, Guo Y. Large-eddy simulation of turbulent flow considering inflow wakes in a Francis turbine blade passage. *Journal of Hydrodynamics*, *Series B* 2007; **19**:201–209.
4. Mahesh K, Constantinescu G, Moin P. A numerical method for large-eddy simulation in complex geometries. *Journal of Computational Physics* 2004; **197**:215–240.
5. Smagorinsky J. General circulation experiments with the primitive equations. *Monthly Weather Review* 1963; **91**:99–164.
6. Bardina J, Ferziger J, Reynolds W. Improved subgrid scale models for large eddy simulation. *AIAA Paper* 1980; **80**:1357.
7. Piomelli U, Moin P, Ferziger JH. Model consistency in large eddy simulation of turbulent channel flows. *Physics of Fluids* 1988; **7**:1884–1891.
8. Germano M, Piomelli U, Moin P *et al*. A dynamic subgrid-scale eddy viscosity model. *Physics of Fluids* 1991; **3**:1760–1765.
9. Lilly DK. A proposed modification of the Germano subgrid-scale closure method. *Physics of Fluids A* 1992; **4**(3):633–635.
10. Zang Y, Street R, Koseff J. A dynamic mixed subgrid-scale model and its application to turbulent recirculating flows. *Physics of Fluids* 1993; **5**:3186–3196.
11. Sarghini F, Piomelli U. Scale-similar models for large-eddy simulations. *Physics of Fluids* 1999; **11**:1596–1607.
12. Ghosal S, Moin P. The basic equations for the large eddy simulation of turbulent flows in complex geometry. *Journal of Computational Physics* 1995; **118**:24–37.
13. Davidson L. Large eddy simulation: a dynamic one-equation subgrid model for three-dimensional recirculating flow. *11th International Symposium on Turbulent Shear Flow*, Grenoble, vol. 3, 1997; 26.1–26.6.
14. Krajnovic S, Davidson L. Large-eddy simulation of the flow around a surface-mounted cube using a dynamic oneequation subgrid model. In *The First International Symposium on Turbulence and Shear Flow Phenomena*, Banerjee S, Eaton J (eds.), Begell House Inc: New York, Wallingford, U.K., 1999; 741–746.
15. Krajnovic S, Davidson L. Large eddy simulation of the flow around a three-dimensional bluff body. *39th AIAA Aerospace Sciences Meeting and Exhibit*, *AIAA Paper* 0432, Reno, NV, U.S.A., 2001.
16. Sohankar A, Davidson L, Norberg C. Large eddy simulation of flow past a square cylinder: comparison of different subgrid scale models. *ASME*: *Journal of Fluids Engineering* 2000; **122**(1):39–47.
17. Sohankar A, Davidson L, Norberg C. Erratum. *ASME*: *Journal of Fluids Engineering* 2000; **122**(3):643.
18. Martinuzzi R, Tropea C. The flow around surface-mounted prismatic obstacles placed in a fully developed channel flow. *ASME: Journal of Fluids Engineering* 1993; **115**:85–91.
19. Krajnovic S, Davidson L. A mixed one-equation subgrid model for large eddy simulation. *International Journal of Heat and Fluid Flow* 2002; **23**:413–425.
20. Moin P. Advances in large eddy simulation methodology for complex flows. *International Journal of Heat and Fluid Flow* 2002; **24**:710–720.
21. Conway S, Caraeni D, Fuchs L. Large eddy simulation of the flow through the blades of a swirl generator. *International Journal of Heat and Fluid Flow* 2002; **21**:664–673.
22. Tyagi M, Acharya S. Large eddy simulation of turbulent flows in complex and moving rigid geometries using the immersed boundary method. *International Journal for Numerical Methods in Fluids* 2005; **48**:691–722.
23. Wu XH, Durbin PA. Evidence of longitudinal vortices evolved from distorted wakes in a turbine passage. *Journal of Fluid Mechanics* 2001; **446**:199–228.

DOI: 10.1002/fld

24. Wissink JG. DNS of separating low Reynolds number flow in a turbine cascade with incoming wakes. *International Journal of Heat and Fluid Flow* 2003; **24**:626–635.
25. Rodi W. DNS and LES of some engineering flows. *Fluid Dynamics Research* 2006; **38**:145–173.
26. Rodi W. A new algebraic relation for calculating the Reynolds stresses. *ZAMM* 1976; **56**:T219–T221.
27. Breuer M, Rodi W. Large eddy simulation of complex turbulent flows of practical interest. In *Flow Simulation with High Performance Computers II*, Notes on Numerical Fluid Mechanics, vol. 52. Hirschel E (ed.). Vieweg: Braunschweig, 1996; 258–274.
28. Nie JH, Armaly BF. Three-dimensional convective flow adjacent to backward-facing stepeffects of step height. *International Journal of Heat and Mass Transfer* 2002; **45**:2431–2438.
29. Nie JH, Armaly BF. Reattachment of three-dimensional flow adjacent to backward-facing step. *ASME Journal of Heat Transfer* 2003; **125**:422–428.
30. Armaly BF, Li A, Nie JH. Measurements in threedimensional laminar separated flow. *International Journal of Heat and Mass Transfer* 2003; **125**:422–428.
31. Nie JH, Armaly BF. Reverse flow regions in three-dimensional backward-facing step flow. *International Journal of Heat and Mass Transfer* 2004; **47**:4713–4720.
32. Sergent E. Vers une Méthodologie de Couplage entre la Simulation des Grandes Echelles et les Modèles Statistiques. *Ph.D. Thesis*, L'Ecole Centrale de Lyon, 2002.

DOI: 10.1002/fld